Applied Surface Science xxx (xxxx) xxx-xxx

Contents lists available at ScienceDirect

Applied Surface Science

journal homepage: http://ees.elsevier.com

Full length article

Hydrothermal synthesis of BiOBr and BiOBr/CNT composites, their photocatalytic activity and the importance of early $Bi_6O_6(OH)_3(NO_3)_3{\cdot}1.5H_2O$ formation

Nikita Sharma [a], Zsolt Pap [b,c,*], Seema Garg [d], Klára Hernádi [a,**]

[a] Department of Applied and Environmental Chemistry, University of Szeged, H–6720 Rerrich Béla 1, Szeged, Hungary
[b] Institute of Environmental Science and Technology, University of Szeged, H-6725, Tisza Lajos 103, Szeged, Hungary
[c] Nanostructured Materials and Bio-Nano-Interfaces Centre, Institute for Interdisciplinary Research on Bio-Nano-Sciences, Babeș–Bolyai University, RO400271, Treboniu Laurian 42, Cluj-Napoca, Romania
[d] Department of Chemistry, Amity Institute of Applied Sciences, Amity University, Sector-125, Noida U.P. 201313, India

ARTICLE INFO

Keywords
Bismuth oxyhalides
BiOBr
Photocatalysis
MWCNTs
Hydrothermal synthesis
Visible light
Phenol

ABSTRACT

Bismuth oxybromide (BiOBr) is a novel visible light photocatalyst and when combined with multiwalled carbon nanotubes (CNT), it could lead to low electron/hole recombination rates, thus enhancing its photocatalytic activity. In this work, hierarchal BiOBr and BiOBr/CNT composites were successfully synthesized via hydrothermal method. The samples prepared were characterized for structural, morphological and optical properties via XRD, SEM, TEM and DRS. The influence of carbon nanotubes on various properties of BiOBr were studied and correlated. The impact of synthesis parameters (time and temperature) on structural properties was also studied. The photocatalytic degradation of phenol as model pollutant was carried out under visible light source to determine its photocatalytic activity. It was found that the presence of CNTs induced a growth in the crystallite size of the particles, which somewhat lowered the photocatalytic activity. As the CNT content increased in the sample so does the activity , due to the CNTs' visible light absorption capacity. Furthermore, a crystal orientation changes (crystallographic plane of (003)) were induced by varying several parameters, which were found to be influencing the activity as well, while the formation of $Bi_6O_6(OH)_3(NO_3)_3{\cdot}1.5H_2O$ was also observed. Its presence enhanced the photocatalytic activity but induced an instability problem.

1. Introduction

Environmental contamination of air, water and land has resulted from many human activities [1–4]. The conventional methods for remediation such as adsorption with active coal and filtration are useful, but inadequate for some of the more challenging persistent contaminants like organic pollutants such as phenols, dyes and pesticides. [5–7]. For example, physico-chemical processes like coagulation and flocculation, when applied to different chemical agents (chlorides of aluminum or iron, or polyelectrolytes etc.), leads to the generation of sludge [8]. Photocatalysis is considered the most promising, effective, and "greener" technique [9–11] for eliminating toxic and recalcitrant organic pollutants from the environment by complete mineralization of such pollutants under mild conditions [12–14]. Other applications of photocatalysis include production of hydrogen by electrochemical water splitting [15], reduction of CO_2 into organic substances [16,17], nitrogen fixation, sterilization [18,19], self-cleaning glasses [20–23] and heavy metal removal from water [14,24–26]. The traditionally used semiconductor photocatalyst, titanium dioxide (TiO_2) [23], although an affective photocatalyst, is only able to take advantage of ultraviolet light which comprises of 4% of total solar energy due to its wide band-gap (3.2 eV for anatase) [11,27–29]. This limits its practical application [20,30]. Visible light driven photocatalysts should be developed which would be able to make use of the rest of 43% of visible region in the solar spectrum [31,32].

Several classes of visible light photocatalyst are being investigated and modified [17,30,33–37], but bismuth oxyhalides, (BiOX, X = Cl, Br, I), due to their unique layered structure [38,39], suitable band gap values, and stability [40,41] has shown promising visible light response [28,42]. They have relative stability under UV/visible light irradiation, show visible light active response and superior performance

* Correspondence to: Z. Pap, Institute of Environmental Science and Technology, University of Szeged, H-6725, Tisza Lajos 103, Szeged, Hungary.
** Corresponding author.
E-mail addresses: pzsolt@chem.u-szeged.hu (Z. Pap); hernadi@chem.u-szeged.hu (K. Hernádi)

https://doi.org/10.1016/j.apsusc.2019.143536
Received 18 Febraury 2019; Received in revised form 13 July 2019; Accepted 30 July 2019
Available online xxx
0169-4332/

compared to Evonik Aeroxide P25 (titania) under UV irradiation [31,43].

BiOBr is now widely used as photocatalysts in degrading pollutants including dyes such as (Methyl Orange, Rhodamine B, Methylene Blue, etc.) [12,44,45], phenols [46], some phenolic compounds [3], and for some pesticides [47]. These are among the best choices when it comes to visible light photocatalytic activity due to its high photocorrosion stability and high photoactivity [48], its good chemical stability and non-toxicity [49], and the low probability of charge carrier recombination [50]. Despite these advantages, the overall photocatalytic efficiency of BiOBr is still low for practical applications [49,51].

Two major challenges for many photocatalysts, including BiOBr, are the prevention of recombination of electrons and holes [52], and efficient harvesting of solar energy [53], both of which drastically affect the photocatalytic activity. One way to remediate these problems is by doping or preparing composites materials. For example, boron doped BiOBr nanosheets were shown to inactivate *E. coli* K-12 using fluorescence tubes as visible light source [54]. In another report, BiOBr was combined with other semiconductors (such as CeO_2, WO_3, $CaFe_2O_4$) to form heterojunctions [17]. There are also reports of modifying properties by using of carbon/carbon-based materials such as graphene or graphene oxide [17,55], and carbon nanotubes. Due to their unique electrical and high mechanical properties, CNTs can serve best in combination with different photocatalysts, especially bismuth-based ones [56]. Hence, these are now considered as one of the promising materials in environmental cleaning. Other successful tuning of BiOBr's properties has also been reported [41,53,57–61]. In particular, TiO_2/MWCNT composite was able to degrade oxalic acid and phenol [62]. Similarly, there are other reports which have marked the excellence of MWCNTs in the field of photocatalysis [56,63–66]. Therefore, it is plausible that MWCNTs could also be paired with BiOBr to study their role in degrading pollutants such as phenol effectively.

In all the references quoted above, only the theoretical aspect of carbon nanotubes have been mentioned and is attributed to its electron storage ability, thus acting as a charge separation material. This, in the end, is reported as one of the causes of enhanced photocatalytic activity of the photocatalyst. On the other hand, there are still voids in the areas of semiconductors grown on carbon nanotubes and how its growth on CNTs influences the physical, chemical and optical properties of the photocatalysts. This is the field which is still undiscovered and has a lot to research about. The answers to such questions related to carbon nanotubes as crystallization support and their impact on morpho-structural changes of the composites are yet to find.

In this work, we have synthesized BiOBr/MWCNT composites via hydrothermal synthesis at two different time and temperature conditions. We have investigated the influence of MWCNT together with synthesis parameters on structural and optical properties (such as crystal orientations, band gap and photocatalytic activity) of the BiOBr/MWCNT composites.

2. Experimental

2.1. Materials

Bismuth nitrate pentahydrate [Bi $(NO_3)_3{\cdot}5H_2O$] purchased from Sigma–Aldrich, 98.0%, glacial acetic acid, 100% purchased from Molar Chemicals Kft. and potassium bromide [KBr], 99.0% purchased from Reanal, Phenol (VWR extra pure, 100%) was purchased from VWR. Deionized water was used for the entire study. All the reagents were of analytical grade and used without further purification.

2.2. Sample preparation

2.2.1. Synthesis of BiOBr

For the synthesis of BiOBr, bismuth nitrate pentahydrate (1 mM in the final synthesis mixture, 3.0 g) was dissolved in 3 mL glacial acetic acid with slight heating (40–45 °C) to decrease the dissolution time. This solution was added to 25 mL deionized water (marked as solution A) and was stirred until it was well dispersed. For solution B, potassium bromide (1 mM in the final synthesis mixture, 0.78 g) was dissolved in 25 mL deionized water under magnetic stirring until it was completely dissolved. Further, solution A was added to solution B dropwise and the mixture was stirred for 20 min to ensure completion of the reaction. A yellow precipitate appeared which was transferred to a stainless-steel, Teflon lined autoclave and subsequently heated at two different time and temperature conditions (120 °C & 150 °C for 4:30 h and 6:30 h each.). It was then cooled down to room temperature (naturally) and the product was collected and washed with ethanol and deionized water three times each using centrifugation at 4400 rpm for 5 min. The final product was dried at 60–80 °C in a vacuum furnace overnight.

2.2.2. Synthesis of BiOBr/MWCNT composite

BiOBr/MWCNTs composites were prepared in a similar manner, except the MWCNTs were added to solution A prior mixing of the two solutions (A and B). Therefore, after adding desired % content of MWCNTs (0.5%, 1%, 2% - values in weight percentage), solution A was sonicated for 2 h, during which a black colored suspension was formed. This was now solution A with MWCNTs, while solution B was prepared similarly as mentioned before and the same procedure follows.

2.3. Characterization

The products were characterized by X-Ray diffraction (XRD) using a Rigaku Miniflex II diffractometer ($2\theta^\circ = 10–80^\circ$, λ (CuK_α) = 0.15418 nm) equipped with a graphite monochromator for the analysis of the structural properties of the composites. The mean primary crystallite size was calculated using the Scherrer equation. N_2 adsorption-desorption measurements were carried out to measure the specific surface areas of the samples, according to the BET (Brunauer-Emmett-Teller) method. To examine the morphology of the composites, Scanning Electron Microscopy (SEM) and Transmission Electron Microscopy (TEM) were used. For TEM measurements, a small amount of sample was dispersed in ethanol with the aid of ultrasonication for about 10 min followed by dropping small drops of the suspension onto a Cu TEM grid (Electron Microscopy Sciences, CF200-Cu). The optical properties were analyzed using Diffuse Reflectance Spectroscopy (UV–vis-DRS) JASCO-V650 with an integration sphere (ILV-724) (λ = 300–800 nm). The indirect band-gap energy was calculated using the Kubelka-Munk equation, while the first derivative spectrum ($dR/d\lambda$) was also obtained and analyzed [67].

2.4. Photocatalytic measurements

The photocatalytic activity of the composites was measured by the degradation of a phenol aqueous solution. A photoreactor system with 4×24 W visible light lamps (irradiation time = 4:00 h) was used to measure the photocatalytic activities under thermostatic (25 °C) conditions using 1 M sodium nitrite solution to eliminate any UV light, which may alter the results. The photocatalyst suspension containing the pollutant was continuously purged with air to keep the dissolved oxygen concentration constant during the whole experiment. The initial concentration of phenol (C_0) was 0.1 mM and the amount of catalyst loaded was $1.0\,g{\cdot}L^{-1}$ with 130 mL total volume of the suspension (V_{susp}). The suspension was treated by ultrasonication for 5 min. After

initial 30 min of stirring in dark to ensure the establishment of adsorption-desorption equilibrium, the samples were withdrawn every 10 min. for the next 60 min. and then every 20 min. for the next 180 min. The samples collected were centrifuged for 3 min. at 15000 rpm and filtered with Filtratech 0.25 μm syringe filter. The decrease in concentration of the model pollutant (phenol) and its primary degradation intermediates were measured by HPLC (Merck-Hitachi L-7100) with a low-pressure gradient pump, equipped with a Merck-Hitachi L-4250 UV–Vis detector and a Lichrospher R_p 18 column using a methanol/water (50:50 v/v) mixture as eluent and 210 nm as the detection wavelength. The TOC (total organic carbon) analysis was carried out using an Analytik Jena multi N/C®3100 apparatus equipped with NDIR detector. The furnace temperature was 800 °C and 1.0 cm^3 samples were injected. Three parallel measurements were made in each case, while COD (chemical oxygen demand) was measured using the well-known bichromate method.

3. Results and discussions

3.1. XRD and N_2 adsorption measurements

Both pure BiOBr and composite samples showed the diffraction peaks for pure BiOBr (tetragonal phase, JCPDS file number 09-0393) [68] when analyzed by XRD (see Fig. 1). The characteristic peaks for MWCNT were not visible due to their low content, such as the one at 2θ = 26.1° [JCPDS 41-1487], the diffraction peak of MWCNTs overlap with that of BiOBr. There were no observed shifts in the peak positions of composite samples, indicating that the lattice structure of BiOBr did not change upon the addition of MWCNTs. Crystallite size increased from 33.8 nm to 60.9 nm in the case of prolonged hydrothermal treatment (from 4:30 h to 6:30 h) and from 33.75 nm to 102.05 nm in the cases of increased hydrothermal temperature from 120 °C to 150 °C at 4:30 h. This is consistent with other reports [31] as well. Fig. 1 shows the diffractograms of composites prepared at 120 °C at 4:30 h with different % MWCNTs.

Additional peaks were observed in nearly all the samples at 10.3, 21.4, 24.6 and 31.3 (2θ°) values, which were identified as $Bi_6O_6(OH)_3(NO_3)_3{\cdot}1.5H_2O$ (JCPDS file number 53-1038). The appearance of this product was rather surprising, but the reason which leads to this compound is not known. As $Bi(NO_3)_3{\cdot}5H_2O$ was the precursor it can be imagined that the first hydrolytic step of the salt occurs by forming this structure. Furthermore, it disappears (maximum content calculated was 8.23 wt% - BiOBr + 0%CNT@120_4:30) as the crystallinity degree of the samples are increasing (e.g. with the increase of the carbon nanotube content - visible also by the increased diffraction peak intensity values in the presence of CNTs, or with the increase of the crystallization time). Furthermore, it should be noted, that this material is considered as a photocatalyst [69] (see Fig. 2).

The BET calculated specific surface areas of the samples varied with changes in hydrothermal synthesis parameters (time and temperature). These measurements confirmed that all the samples have low surface area in agreement with the higher crystallite size as calculated from XRD data. The specific surface area ranges from 2.3 m^2/g to 7.3 m^2/g.

3.2. Morphology analysis

SEM was applied to verify the morphology of the samples. For all the composites, microplate-like structure was obtained. MWCNTs in the composites were found to be in close contact with the microplates (Fig. 3(c)) and from the investigated sample areas it seems that they were not homogeneously distributed throughout the sample. Fig. 3 shows SEM micrographs of the samples prepared at 150 °C and 4:30 h. As in addition to the BiOBr microplates, the surface of MWCNTs were covered with the nanoparticles of photocatalyst (see Fig. 3(c)). Applying a prolonged hydrothermal treatment, there was decrease in thickness of microplates between 133 and 145 nm in case of 150 °C at 4:30 h and 6:30 h, respectively (from Fig. 3(a) and (b)) and between 55 and 78 nm in case of 120 °C at 4:30 h and 6:30 h, respectively. This decrease in thickness may be later correlated with the samples' orientation as well.

3.3. DRS measurements

The band gap energy (E_g) of the composites was reduced from 2.87 and 2.84 eV to 2.41 eV with increasing MWCNTs content. This may be due to the light absorption capacity of MWCNTs that absorbs the available electromagnetic radiation (black color of MWCNTs), as the color

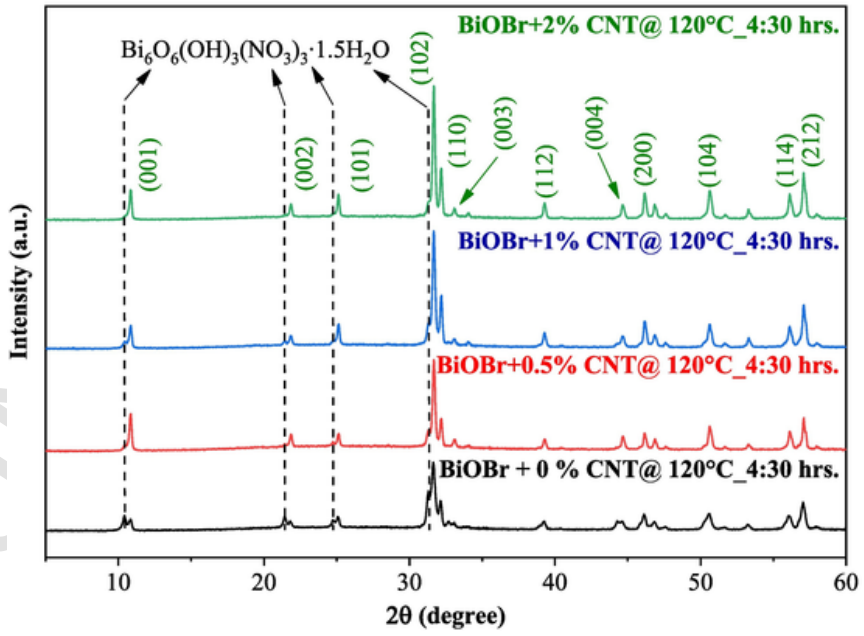

Fig. 1. X-ray diffractograms of BiOBr/MWCNTs composites with different % MWCNTs prepared at 120 °C @ 4:30 h. Peaks are indexed to BiOBr tetragonal phase (JCPDS file number 09-0393), while $Bi_6O_6(OH)_3(NO_3)_3{\cdot}1.5H_2O$ also appeared.

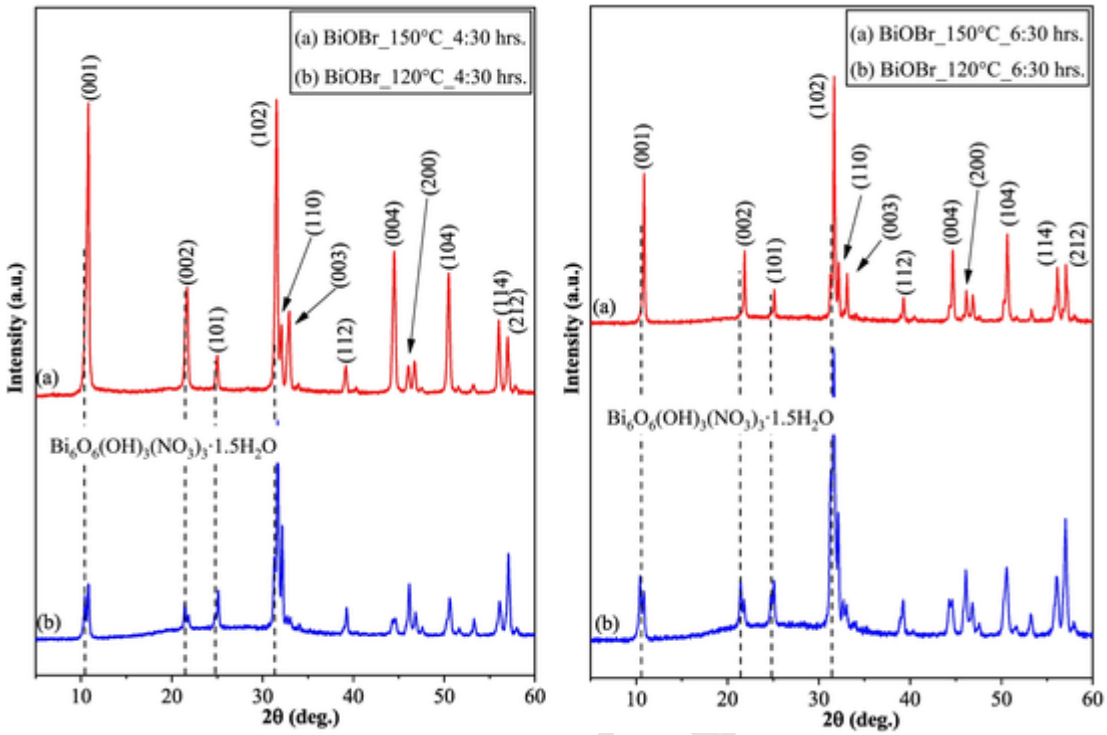

Fig. 2. X-ray diffractograms of BiOBr prepared at 120 °C (left) and 150 °C (right) @ 4:30 and 6:30 h.

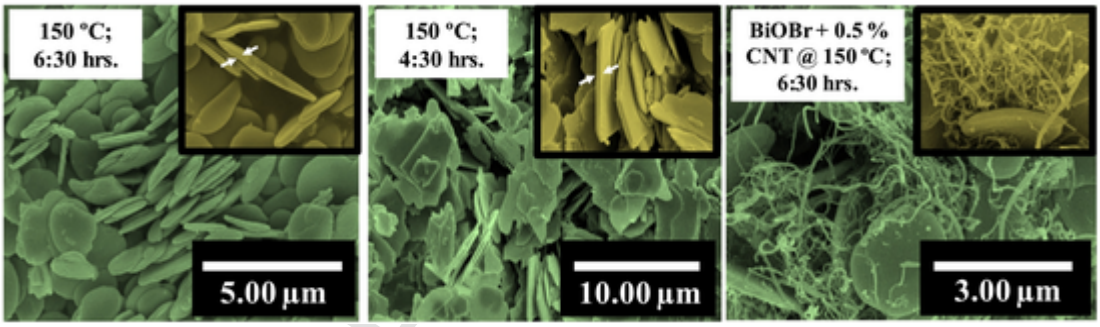

Fig. 3. SEM micrographs of BiOBr synthesized at 150 °C (a) 6:30 h and (b) 4:30 h (c) 0.5% CNT at 6:30 h.

of the samples suggested. The band gap decrease also suggests the separation of charge carriers with low probability of recombination, although a short-circuiting mechanism is also known for these composites. Even though, a decrease in band-gap energy of the samples was found using Kubelka-Munk Theory but through the first derivative, no shift in the absorption spectrum was found which means that the decreased E_g values reported, were not the actual band-gap values of the composites. These represent somewhat misleading values of the band gap energy of the composites but indicate the overall band-properties.

Further analyzing the band structure of the materials, the first derivative spectra of the samples were investigated. It was found that, in all the cases two electro transition bands (Fig. 4) were observed in nearly all the cases, one at 3.3 eV (electron transition band located at 385 nm) and one at 2.9 eV (electron transition band located at 422 nm). The band at 2.9 eV belongs to BiOBr, but the second one was not expected. However, in Section 3.1 it was found that $Bi_6O_6(OH)_3(NO_3)_3{\cdot}1.5H_2O$ was present in the samples. The band gap value reported in the literature coincides with the second electron transition band identified here at 3.3 eV. Furthermore, this signal is omnipresent in all the samples as $Bi_6O_6(OH)_3(NO_3)_3{\cdot}1.5H_2O$ is also present but in different amounts. This shows, that this compound will participate in the charge separation mechanism, during the photocatalytic experiments.

3.4. Photocatalytic evaluation and its relationship with other parameters

Fig. 5 shows the photocatalytic degradation of phenol in presence of different composites under visible light irradiation. Unlike composite systems reported elsewhere [70], the samples without MWCNTs showed the enhanced photocatalytic degradation of phenol as compared to the composites containing different amount of MWCNTs. The trends as expected from the theoretical information and literatures mentioned previously, were not observed with the addition of MWCNTs even at low concentration into BiOBr. Therefore, it can be affirmed that, one major trend is clearly visible from Fig. 5, that increasing the MWCNT content lowered the photoactivity, except in the case of the samples obtained at 150 °C (4:30), where no precise activity order can be defined.

Thus, it is clear here, that the MWCNTs do not contribute in trapping the electrons and promoting charge separation among the photocatalyst in our case. All the samples without MWCNTs prepared at 120 °C and 150 °C showed the highest photocatalytic activity (Fig. 6)

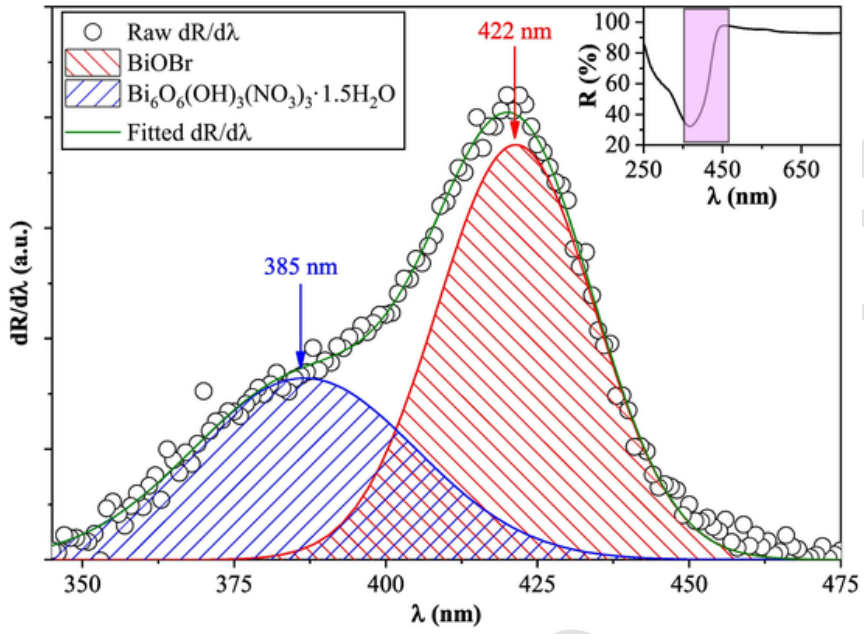

Fig. 4. First derivative DRS spectrum of sample BiOBr + 0%CNT@120_4:30, showing two electron transition bands, which can be associated to the two products obtained from the solvothermal synthesis.

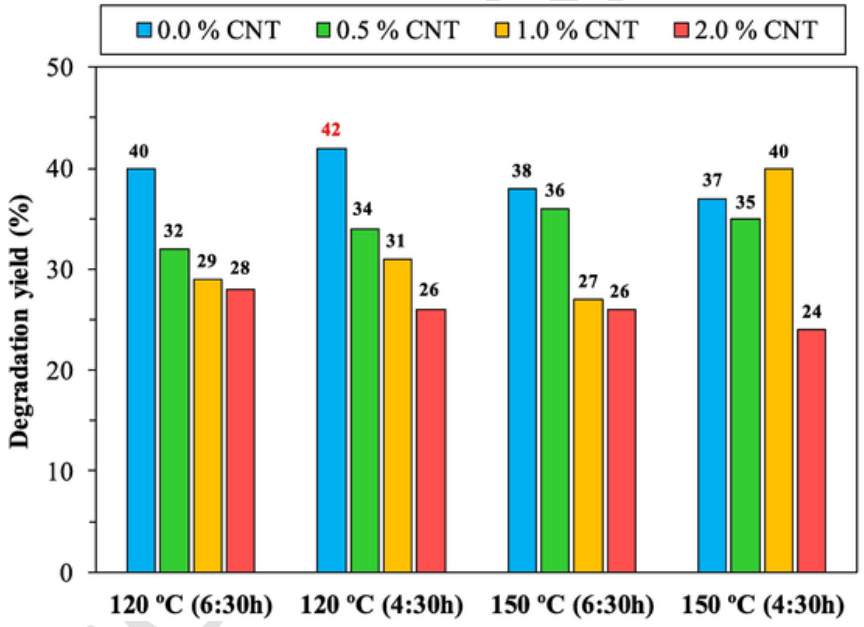

Fig. 5. Trends in the degradation yield after 4 h with respect to MWCNTs content and hydrothermal synthesis parameters (time and parameters).

for phenol under visible irradiation with 42% as degradation efficiency for the sample synthesized at 120 °C at 4:30 h.

To gain insights about the nature of the photoactivity of the samples several correlations were made. The first one was the amount of MWCNTs discussed earlier. The second one could be the primary crystallite size, a well-known parameter [71], which was deeply discussed in the literature (e.g. for TiO_2). Usually, with the crystallite size decrease an activity increase was noticed, which is logical as the specific surface area values were increasing as well. However, in the present case we must deal with very low values (below 10 m^2/g). The photocatalytic degradation efficiencies showed also two types of dependencies:

- As expected, as the primary crystallite size was increasing (see Fig. 7), the degradation efficiency of the photocatalysts decreased, but after 80 nm particle size, the degradation values began to increase again for the samples obtained at 150 °C
- The samples obtained at 120 °C did not show the changes in the trend as it was in the case of the samples obtained at 150 °C.

These two observations pointed out that some structural changes may occur in the samples obtained at 150 °C, which showed high (not the highest) activity at high primary crystallite size values.

Fig. 8 shows the experimental data between the band gap energy values (in eV) with the degradation efficiency (% deg.). Although, a decrease in the band gap values was observed with the addition of MWCNTs, it did not contribute to the enhancement of photocatalytic activity, fact already observed in the case of titania photocatalyst doped with nitrogen [72]. BiOBr prepared at 120 °C at 6:30 and 4:30 h had

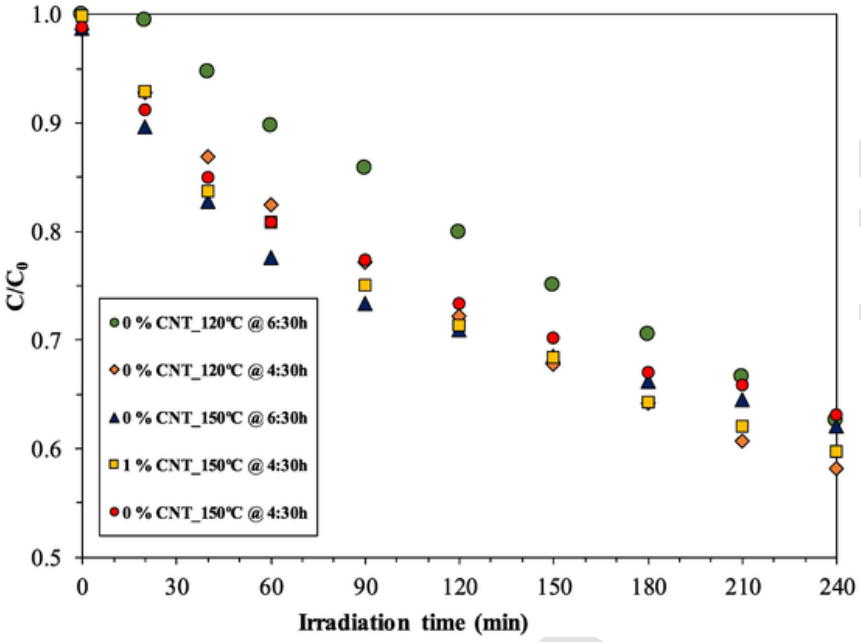

Fig. 6. Photocatalytic degradation of phenol by selected samples under visible light irradiation.

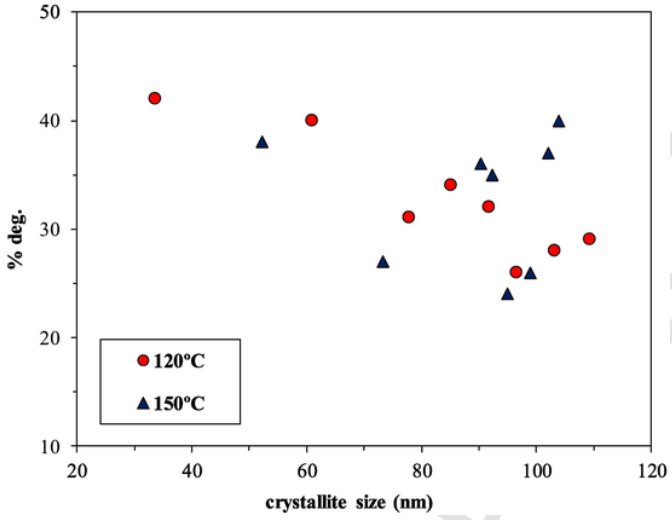

Fig. 7. Correlation between the primary crystallite size (nm) with the degradation efficiency (% deg.) of phenol under visible light irradiation.

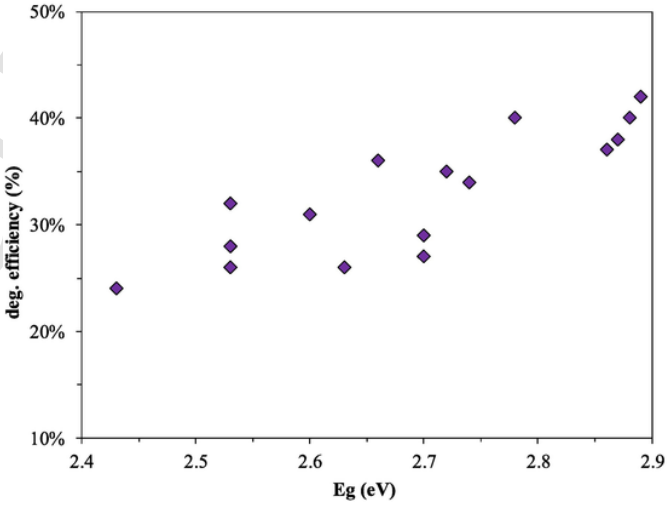

Fig. 8. Correlation between the band gap values (eV) with the photocatalytic degradation of phenol under visible light irradiation.

E_g = 2.84 eV with the highest photodegradation efficiency of 40% and 42%, respectively, while the lowest band gap value (E_g) of 2.41 eV was obtained for the composite containing 0.5% MWCNT with low photodegradation efficiency of 26% achieved.

However, this fact is very well supported from the data obtained from the first derivative DRS. As the amount of $Bi_6O_6(OH)_3(NO_3)_3{\cdot}1.5H_2O$ increases (from 1.52% to 8.23%) so does the band-gap of the catalyst and with it the visible light driven phenol photodegradation. It should be remembered that those materials which had the lower carbon nanotube content were the ones with the high $Bi_6O_6(OH)_3(NO_3)_3{\cdot}1.5H_2O$ content. As the nanotube content increased the formation of BiOBr was favored instead of $Bi_6O_6(OH)_3(NO_3)_3{\cdot}1.5H_2O$.

Not just the presence of a specific compound would influence the activity. As these are shape-tailored materials the crystal orientation could also show the origin of the activity. That is why all the important diffraction peaks were indexed. One significant correlation was observed, that of facet (003). In the literature (120), (110) and (102) are among the facets found responsible for the photoactivity. This was not the case here. The presence of (003) inhibited the activity of the samples until the ratio of (0.075), after that a constant increase of activity with the presence of (003) was noticed. In Fig. 9 subseries values were denoted with different colors, which show that except for sample series without CNT all the others aligned perfectly with the beneficial effect of (003). The highest amount of MWCNT (2%) showed the lowest (003) presence, emphasizing again, the effect of crystallization promoter agent of MWCNT, while the other MWCNT concentration values produced higher amount of the desired crystallographic plane. Furthermore, the two samples with very low (003) crystallographic ratio which were very active contained in the highest amount of $Bi_6O_6(OH)_3(NO_3)_3{\cdot}1.5H_2O$, which is why they are not part of the increasing activity trend in function of the presence of (003).

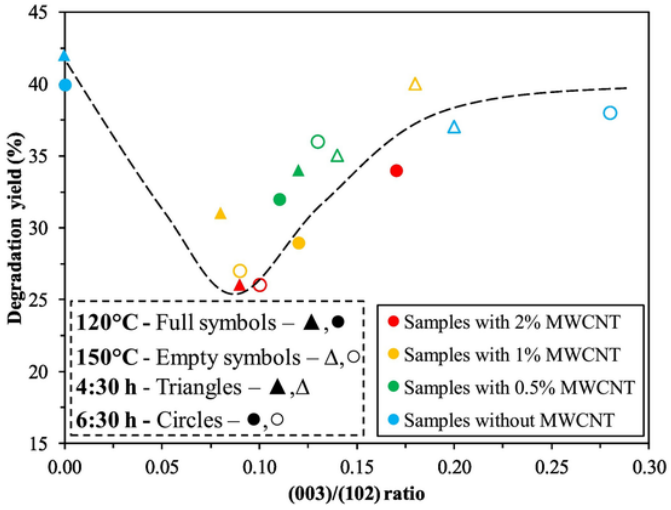

Fig. 9. Correlation between (003)/(102) crystallographic planes' ratio with the photocatalytic degradation of phenol under visible light irradiation.

3.5. Stability and photoactivity of the samples

In all the cases the question of stability arises, as always. To verify the stability and reusability of the investigated materials were tested under the conditions mentioned in the experimental section. The first step was to check the COD and TOC removal rate of the best performing material in order to verify if a constant decrease is visible or not. Surprisingly the mentioned values did not change at all (Fig. S1), suggesting that during the degradation an inhibition mechanism or a poisoning process was underway, which did not permit the total mineralization of phenol.

As shown in the previous sections the obtained photocatalysts showed specific morphology, thus the next experiment was to verify the morphological stability after 3 successive photocatalytic runs of the best 3 samples for phenol degradation under the same conditions. At the first glance, no changes were observed in the SEM micrographs (Fig. 10), meaning that the same plate-like morphology was obtained. Consequently, the concentration evolution of phenol was evaluated during the 3 photodegradation cycles (Fig. 11). It was found that the photoactivity of all the tested samples was lowered after each test. The overall activity loss was around 50% and in one case activity regain was also observed (sample BiOBr + 1%CNT@150_4:30). The latter observations are rather interesting and further investigations are needed to clarify this issue.

If no changes were observed in the morphology, the only explanation must lie in the crystal structure of the samples. The XRD patterns (Fig. 12) of the studied samples showed significant changes. First, the $Bi_6O_6(OH)_3(NO_3)_3{\cdot}1.5H_2O$ related diffraction peaks totally disappeared, only the signals of BiOBr remained, emphasizing the recrystallization hypothesis mentioned at the beginning of this section. The (001) crystallographic plane did not give any signals in the reused material, pointing out a morphology preservation but total recrystallization, which was supported by the lower crystallinity grades and primary crystallite size values (a lowering of almost 50% in size, achieving values between 10.2 and 24.5 nm). Moreover, the important (003) crystallographic plane disappeared in all the samples (except for BiOBr + 1%CNT@150_4:30, but also here its ratio was quite low). However, in the exception sample was registered the only activity increase which is a new and direct evidence that the formation of (003) is beneficial.

4. Conclusion

The BiOBr samples obtained using different crystallization parameters and in the presence of MWCNT showed interesting results. The growth of $Bi_6O_6(OH)_3(NO_3)_3{\cdot}1.5H_2O$ was observed, which was intermediate product, which decreases as the crystallization parameters are favoring further recrystallization processes, to achieve higher crystallinity (high MWCNT content, longer hydrothermal crystallization duration

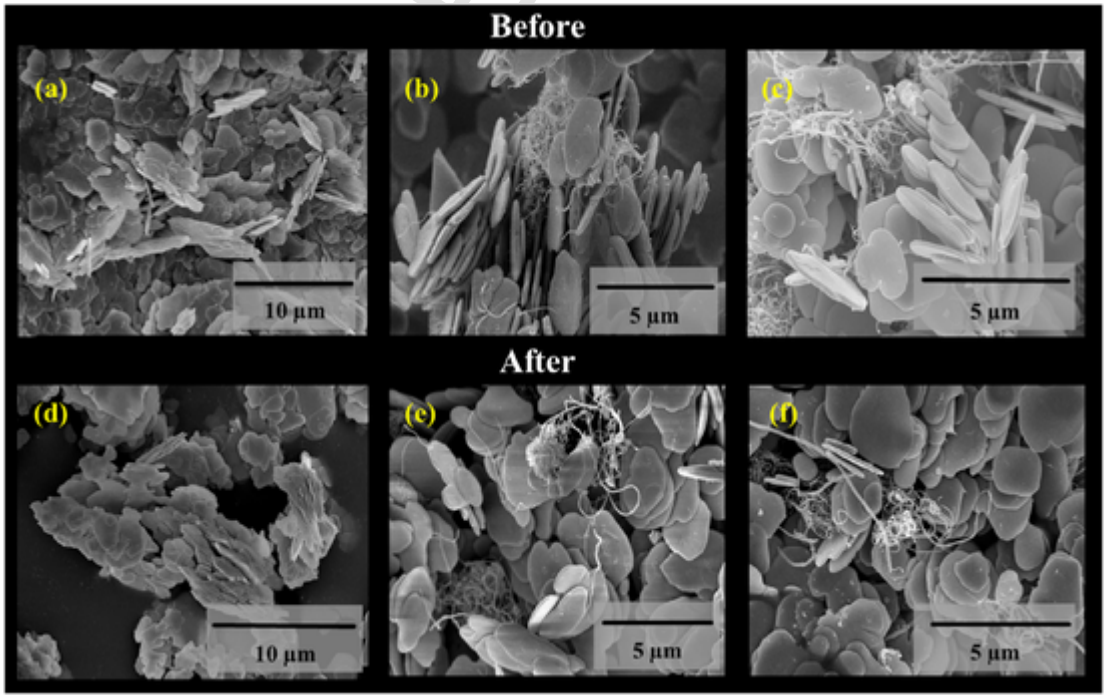

Fig. 10. SEM micrographs of the samples before and after the stability tests. (a), (b), (c) represents samples BiOBr + 0%CNT@120_4:30, BiOBr + 0.5%CNT@150_6:30, BiOBr + 1%CNT@150_4:30 respectively, before the stability test and (d), (e), (f) represents BiOBr + 0%CNT@120_4:30, BiOBr + 0.5%CNT@150_6:30, BiOBr + 1%CNT@150_4:30 respectively, after the stability test.

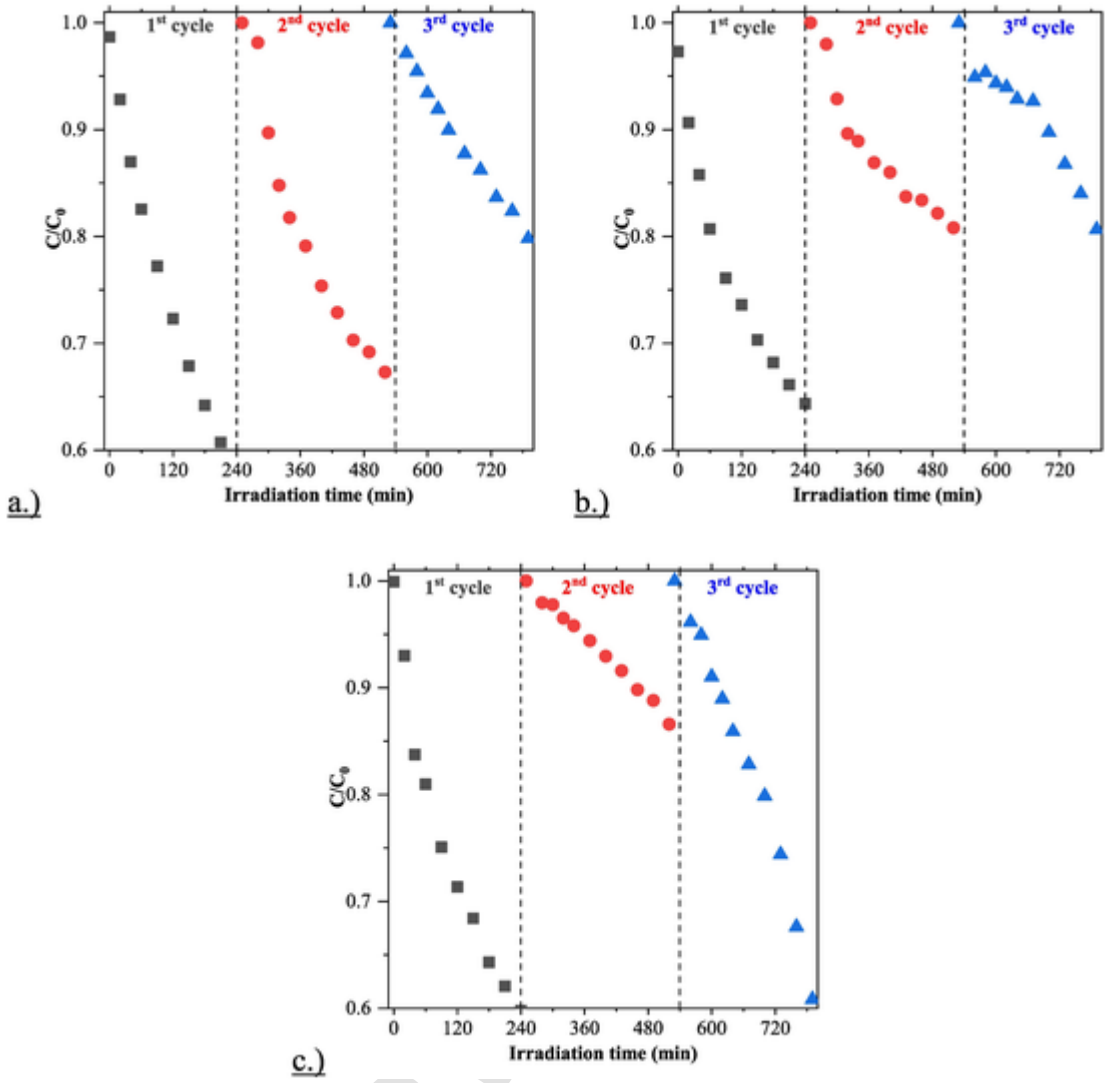

Fig. 11. Photocatalytic reusability tests (3 cycles) of the samples BiOBr + 0%CNT@120_4:30, BiOBr + 0.5%CNT@150_6:30 and BiOBr + 1%CNT@150_4:30.

and higher temperature). This intermediate compound proved to be an efficient component in enhancing the photoactivity, although its exact functioning mechanism needs to be discovered. Also, the presence of $Bi_6O_6(OH)_3(NO_3)_3{\cdot}1.5H_2O$ influenced the band-gap value, causing a blue-shift, while enhancing the photoactivity. The morphology of the particles was plate-like and in some cases where MWCNTs were used, also nanoparticle covered tubes were obtained. The photoactivity of the samples proved to be dependent also on the crystallite size, showing that also at higher primary particle size values, high activity can be achieved. The orientation of the crystals proved to be again a key factor, but a not yet reported (003) facet was responsible in enhancing the overall photoactivity. Furthermore, the above investigated samples showed poor stability, due to morpho-structural changes during irradiation.

Supplementary data to this article can be found online at https://doi.org/10.1016/j.apsusc.2019.143536.

Acknowledgements

This work was supported by the Indo-Hungarian TÉT project (TÉT_15_IN-1-2016-0013) and Department of Science and Technology, Delhi, India (INT/HUN/P-06/2016). Special thanks to Tamás Gyulavári, Gábor Kovács for carrying out SEM and DRS measurements. The authors would like to thank Prof. Arwyn Smalley, for helping in language editing of the article.

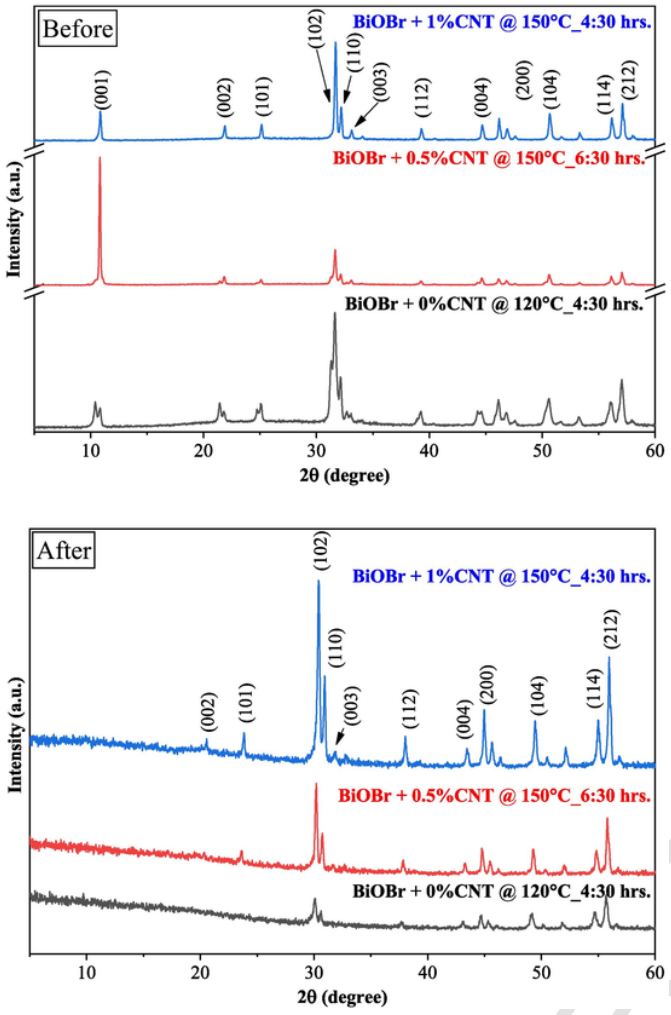

Fig. 12. XRD of the samples before and after the stability tests, showing a change in the crystal orientation, which was concomitant with a decrease in crystallinity grade as well.

References

[1] R. Ameta, S. Benjamin, A. Ameta, S.C. Ameta, Photocatalytic degradation of organic pollutants: a review, Mater. Sci. Forum 734 (2012) 247–272, doi:10.4028/www.scientific.net/MSF.734.247.

[2] V. Binas, D. Venieri, D. Kotzias, G. Kiriakidis, Modified TiO_2 based photocatalysts for improved air and health quality, J. Mater. 3 (2017) 3–16, doi:10.1016/j.jmat.2016.11.002.

[3] A. Han, S.F. Chian, X.Y. Toy, J. Sun, S. Jaenicke, G.K. Chuah, Bismuth oxyiodide heterojunctions in photocatalytic degradation of phenolic molecules, Res. Chem. Intermed. 41 (2015) 9509–9520, doi:10.1007/s11164-015-1976-7.

[4] M.R. Hoffmann, S.T. Martin, W. Choi, D.W. Bahnemann, Environmental applications of semiconductor photocatalysis, Chem. Rev. 95 (1995) 69–96, doi:10.1021/cr00033a004.

[5] A.L.N. Mota, L.F. Albuquerque, L.T.C. Beltrame, O. Chiavone-Filho, A. M Jr., C.A.O. Nascimento, Advanced oxidation processes and their application in the petroleum industry: a review, Brazilian J. Pet. Gas. 2 (2009).

[6] U.G. Akpan, B.H. Hameed, Parameters affecting the photocatalytic degradation of dyes using TiO_2-based photocatalysts: a review, J. Hazard. Mater. 170 (2009) 520–529, doi:10.1016/j.jhazmat.2009.05.039.

[7] P.V.A. Padmanabhan, K.P. Sreekumar, T.K. Thiyagarajan, R.U. Satpute, K. Bhanumurthy, P. Sengupta, G.K. Dey, K.G.K. Warrier, Nano-crystalline titanium dioxide formed by reactive plasma synthesis, Vacuum 80 (2006) 1252–1255, doi:10.1016/j.vacuum.2006.01.054.

[8] A. Elena, C. Orbeci, C. Lazau, P. Sfirloaga, P. Vlazan, C. Bandas, I. Grozescu, Waste water treatment methods, Water Treat (2013), doi:10.5772/53755.

[9] S. Garg, M. Yadav, A. Chandra, K. Hernadi, A review on BiOX (X = Cl, Br and I) nano-/microstructures for their photocatalytic applications, J. Nanosci. Nanotechnol. 19 (2019) 280–294, doi:10.1166/jnn.2019.15771.

[10] L.V. Bora, R.K. Mewada, Visible/solar light active photocatalysts for organic effluent treatment: fundamentals, mechanisms and parametric review, Renew. Sust. Energ. Rev. 76 (2017) 1393–1421, doi:10.1016/j.rser.2017.01.130.

[11] W. Deng, H. Zhao, F. Pan, X. Feng, B. Jung, A. Abdel-Wahab, B. Batchelor, Y. Li, Visible-light-driven photocatalytic degradation of organic water pollutants promoted by sulfite addition, Environ. Sci. Technol. 51 (2017) 13372–13379, doi:10.1021/acs.est.7b04206.

[12] Y. Xie, F. Chang, C. Li, J. Chen, J. Luo, L. Li, X. Hu, One-pot polyvinyl alcohol-assisted hydrothermal synthesis of hierarchical flower-like BiOCl nanoplates with enhancement of photocatalytic activity for degradation of rhodamine B, Clean - Soil, Air, Water 42 (2014) 521–527, doi:10.1002/clen.201300014.

[13] J. Wang, Y. Zhang, L. Tian, F. Liu, Q. Xia, Ultrathin BiOBr nanocrystals with dominant {001} facets and their high photocatalytic activity, J. Nanopart. Res. 16 (2014), doi:10.1007/s11051-014-2691-9.

[14] P. Chowdhury, A. Elkamel, A.K. Ray, CHAPTER 2. Photocatalytic processes for the removal of toxic metal ions, Heavy Met. Water, Royal Society of Chemistry, Cambridge, 2014, pp. 25–43, doi:10.1039/9781782620174-00025.

[15] X. Chen, W. Shangguan, Hydrogen production from water splitting on CdS-based photocatalysts using solar light, Front. Energy. 7 (2013) 111–118, doi:10.1007/s11708-012-0228-4.

[16] S. Nahar, M.F.M. Zain, A.A.H. Kadhum, H.A. Hasan, M.R. Hasan, Advances in photocatalytic CO_2 reduction with water: a review, Materials (Basel) 10 (2017), doi:10.3390/ma10060629.

[17] L. Chen, J. He, Y. Liu, P. Chen, C.T. Au, S.F. Yin, Recent advances in bismuth-containing photocatalysts with heterojunctions, Cuihua Xuebao/Chinese J. Catal. 37 (2016) 780–791, doi:10.1016/S1872-2067(15)61061-0.

[18] A. Vohra, D.Y. Goswami, D.A. Deshpande, S.S. Block, Enhanced photocatalytic disinfection of indoor air, Appl. Catal. B Environ. 64 (2006) 57–65, doi:10.1016/j.apcatb.2005.10.025.

[19] J. Peral, X. Domènech, D.F. Ollis, Heterogeneous photocatalysis for purification, decontamination and deodorization of air, J. Chem. Technol. Biotechnol. 70 (1997) 117–140, doi:10.1002/(SICI)1097-4660(199710)70:2<117::AID-JCTB746>3.0.CO;2-F.

[20] N.R. Khalid, A. Majid, M.B. Tahir, N.A. Niaz, S. Khalid, Carbonaceous-TiO_2 nanomaterials for photocatalytic degradation of pollutants: a review, Ceram. Int. 43 (2017) 14552–14571, doi:10.1016/j.ceramint.2017.08.143.

[21] I.P. Parkin, R.G. Palgrave, Self-cleaning coatings, J. Mater. Chem. 15 (2005) 1689–1695, doi:10.1039/b412803f.

[22] T.-W. Liao, S. Verbruggen, N. Claes, A. Yadav, D. Grandjean, S. Bals, P. Lievens, TiO_2 films modified with Au nanoclusters as self-cleaning surfaces under visible light, Nanomaterials 8 (2018) 30, doi:10.3390/nano8010030.

[23] A. Fujishima, X. Zhang, Titanium dioxide photocatalysis: present situation and future approaches, Comptes Rendus Chim 9 (2006) 750–760, doi:10.1016/j.crci.2005.02.055.

[24] X. Xiong, L. Ding, Q. Wang, Y. Li, Q. Jiang, J. Hu, Synthesis and photocatalytic activity of BiOBr nanosheets with tunable exposed (010) facets, Appl. Catal. B Environ. 188 (2016) 283–291, doi:10.1016/j.apcatb.2016.02.018.

[25] E.F. Pérez-Ramírez, M. de la Luz-Asunción, A.L. Martínez-Hernández, C. Velasco-Santos, Graphene materials to remove organic pollutants and heavy metals from water: photocatalysis and adsorption, Semicond. Photocatal. - Mater. Mech. Appl. (2016), doi:10.5772/62777.

[26] J. Hu, S. Weng, Z. Zheng, Z. Pei, M. Huang, P. Liu, Solvents mediated-synthesis of BiOI photocatalysts with tunable morphologies and their visible-light driven photocatalytic performances in removing of arsenic from water, J. Hazard. Mater. 264 (2014) 293–302, doi:10.1016/j.jhazmat.2013.11.027.

[27] Z. Wei, R. Li, R. Wang, Enhanced visible light photocatalytic activity of BiOBr by *in situ* reactable ionic liquid modification for pollutant degradation, RSC Adv. 8 (2018) 7956–7962, doi:10.1039/C7RA13779F.

[28] Z. Ni, Y. Sun, Y. Zhang, F. Dong, Fabrication, modification and application of $(BiO)_2CO_3$-based photocatalysts: a review, Appl. Surf. Sci. 365 (2016) 314–335, doi:10.1016/j.apsusc.2015.12.231.

[29] Y. Yu, J.C. Yu, J.-G. Yu, Y.-C. Kwok, Y.-K. Che, J.-C. Zhao, L. Ding, W.-K. Ge, P.-K. Wong, Enhancement of photocatalytic activity of mesoporous TiO_2 by using carbon nanotubes, Appl. Catal. A Gen. 289 (2005) 186–196, doi:10.1016/j.apcata.2005.04.057.

[30] F. Huang, A. Yan, H. Zhao, Influences of doping on photocatalytic properties of TiO_2 photocatalyst, Semicond. Photocatal. - Mater. Mech. Appl. (2016), doi:10.5772/63234.

[31] Z. Jiang, F. Yang, G. Yang, L. Kong, M.O. Jones, T. Xiao, P.P. Edwards, The hydrothermal synthesis of BiOBr flakes for visible-light-responsive photocatalytic degradation of methyl orange, J. Photochem. Photobiol. A Chem. 212 (2010) 8–13, doi:10.1016/j.jphotochem.2010.03.004.

[32] Y.P. Moreno, C.C. Escobar, W.L. da Silva, J.H.Z. dos Santos, Alternative approaches in development of heterogeneous titania-based photocatalyst, Semicond. Photocatal. - Mater. Mech. Appl. (2016), doi:10.5772/62891.

[33] Z. Xiang, Y. Wang, D. Zhang, P. Ju, BiOI/$BiVO_4$ p–n heterojunction with enhanced photocatalytic activity under visible-light irradiation, J. Ind. Eng. Chem. 40 (2016) 83–92, doi:10.1016/j.jiec.2016.06.009.

[34] P. Dong, X. Xi, G. Hou, Typical non–TiO_2-based visible-light photocatalysts, Semicond. Photocatal. - Mater. Mech. Appl, InTech, 2016, doi:10.5772/62889.

[35] A.M. Al-Hamdi, M. Sillanpää, J. Dutta, Intermediate formation during photodegradation of phenol using lanthanum doped tin dioxide nanoparticles, Res. Chem. Intermed. 42 (2016) 3055–3069, doi:10.1007/s11164-015-2197-9.

[36] P. Chowdhury, S. Nag, A.K. Ray, Degradation of phenolic compounds through UV and visible-light-driven photocatalysis: technical and economic aspects, Phenolic Compd. - Nat. Sources, Importance Appl, InTech, 2017, doi:10.5772/66134.

[37] D.S. Bhachu, S.J.A. Moniz, S. Sathasivam, D.O. Scanlon, A. Walsh, S.M. Bawaked, M. Mokhtar, A.Y. Obaid, I.P. Parkin, J. Tang, C.J. Carmalt, Bismuth oxyhalides: synthesis, structure and photoelectrochemical activity, Chem. Sci. 7 (2016) 4832–4841, doi:10.1039/C6SC00389C.

[38] H. Zhang, L. Liu, Z. Zhou, Towards better photocatalysts: first-principles studies of the alloying effects on the photocatalytic activities of bismuth oxyhalides under visible light, Phys. Chem. Chem. Phys. 14 (2012) 1286–1292, doi:10.1039/c1cp23516h.

[39] L. Ye, Y. Su, X. Jin, H. Xie, C. Zhang, Recent advances in BiOX (X = Cl, Br and I) photocatalysts: synthesis, modification, facet effects and mechanisms, Environ. Sci. Nano. 1 (2014) 90–112, doi:10.1039/c3en00098b.

[40] Y. Liu, J. Xu, L. Wang, H. Zhang, P. Xu, X. Duan, H. Sun, S. Wang, Three-dimensional BiOI/BiOX (X = Cl or Br) Nanohybrids for enhanced visible-light photocatalytic activity, Nanomaterials 7 (2017) 64, doi:10.3390/nano7030064.

[41] J. Xia, J. Di, S. Yin, H. Xu, J. Zhang, Y. Xu, L. Xu, H. Li, M. Ji, Facile fabrication of the visible-light-driven Bi_2WO_6/BiOBr composite with enhanced photocatalytic activity, RSC Adv. 4 (2014) 82–90, doi:10.1039/c3ra44191a.

[42] K. Natarajan, H.C. Bajaj, R.J. Tayade, Photocatalytic efficiency of bismuth oxyhalide (Br, Cl and I) nanoplates for RhB dye degradation under LED irradiation, J. Ind. Eng. Chem. 34 (2016) 146–156, doi:10.1016/j.jiec.2015.11.003.

[43] J. Liu, L. Ruan, S.B. Adeloju, Y. Wu, BiOI/TiO_2 nanotube arrays, a unique flake-tube structured p-n junction with remarkable visible-light photoelectrocatalytic performance and stability, Dalt. Trans. 43 (2014) 1706–1715, doi:10.1039/c3dt52394b.

[44] F. Chen, H. Liu, S. Bagwasi, X. Shen, J. Zhang, Photocatalytic study of BiOCl for degradation of organic pollutants under UV irradiation, J. Photochem. Photobiol. A Chem. 215 (2010) 76–80, doi:10.1016/j.jphotochem.2010.07.026.

[45] M. Guo, Q. He, A. Wang, W. Wang, Z. Fu, A novel, simple and green way to fabricate BiVO4 with excellent photocatalytic activity and its methylene blue decomposition mechanism, Crystals 6 (2016) 81, doi:10.3390/cryst6070081.

[46] X. Xiao, W.D. Zhang, Facile synthesis of nanostructured BiOI microspheres with high visible light-induced photocatalytic activity, J. Mater. Chem. 20 (2010) 5866–5870, doi:10.1039/c0jm00333f.

[47] A. Dandapat, I. Horovitz, H. Gnayem, Y. Sasson, D. Avisar, T. Luxbacher, H. Mamane, Solar photocatalytic degradation of trace organic pollutants in water by Bi(0)-doped bismuth oxyhalide thin films, ACS Omega 3 (2018) 10858–10865, doi:10.1021/acsomega.8b00759.

[48] Z. Ai, W. Ho, S. Lee, L. Zhang, Efficient photocatalytic removal of NO in indoor air with hierarchical bismuth oxybromide nanoplate microspheres under visible light, Environ. Sci. Technol. 43 (2009) 4143–4150, doi:10.1021/es9004366.

[49] H. Yu, H. Huang, K. Xu, W. Hao, Y. Guo, S. Wang, X. Shen, S. Pan, Y. Zhang, Liquid-phase exfoliation into monolayered BiOBr nanosheets for photocatalytic oxidation and reduction, ACS Sustain. Chem. Eng. 5 (2017) 10499–10508, doi:10.1021/acssuschemeng.7b02508.

[50] Z. Liu, B. Wu, J. Niu, X. Huang, Y. Zhu, Solvothermal synthesis of BiOBr thin film and its photocatalytic performance, Appl. Surf. Sci. 288 (2014) 369–372, doi:10.1016/j.apsusc.2013.10.034.

[51] Y. Huang, B. Long, H. Li, M.S. Balogun, Z. Rui, Y. Tong, H. Ji, Enhancing the photocatalytic performance of $BiOCl_xI_{1-x}$ by introducing surface disorders and Bi nanoparticles as cocatalyst, Adv. Mater. Interfaces 2 (2015) 1–7, doi:10.1002/admi.201500249.

[52] H. Zhao, F. Tian, R. Wang, R. Chen, A review on bismuth-related nanomaterials for photocatalysis, Rev. Adv. Sci. Eng. 3 (2014) 3–27, doi:10.1166/rase.2014.1050.

[53] C. Liu, X. Dong, Y. Hao, X. Wang, H. Ma, X. Zhang, Efficient photocatalytic dye degradation over Er-doped BiOBr hollow microspheres wrapped with graphene nanosheets: enhanced solar energy harvesting and charge separation, RSC Adv. 7 (2017) 22415–22423, doi:10.1039/c7ra02402a.

[54] D. Wu, S. Yue, W. Wang, T. An, G. Li, H.Y. Yip, H. Zhao, P.K. Wong, Boron doped BiOBr nanosheets with enhanced photocatalytic inactivation of Escherichia coli, Appl. Catal. B Environ. 192 (2016) 35–45, doi:10.1016/j.apcatb.2016.03.046.

[55] H. Liu, Y. Su, Z. Chen, Z. Jin, Y. Wang, Graphene sheets grafted three-dimensional $BiOBr_{0.2}I_{0.8}$ microspheres with excellent photocatalytic activity under visible light, J. Hazard. Mater. 266 (2014) 75–83, doi:10.1016/j.jhazmat.2013.12.013.

[56] L.P. Zhu, L.L. Wang, N.C. Bing, P. Li, L.J. Wang, C. Huang, G.H. Liao, In situ synthesis of N-doped carbon nanotubes-BiOCl nanocomposites and their synergistic photocatalytic performance, RSC Adv. 6 (2016) 2926–2934, doi:10.1039/c5ra24149a.

[57] X. Jia, J. Cao, H. Lin, Y. Chen, W. Fu, S. Chen, One-pot synthesis of novel flower-like BiOBr0.9I0.1/BiOI heterojunction with largely enhanced electron-hole separation efficiency and photocatalytic performances, J. Mol. Catal. A Chem. 409 (2015) 94–101, doi:10.1016/j.molcata.2015.08.008.

[58] O. Mehraj, N.A. Mir, B.M. Pirzada, S. Sabir, Fabrication of novel Ag_3PO_4/BiOBr heterojunction with high stability and enhanced visible-light-driven photocatalytic activity, Appl. Surf. Sci. 332 (2015) 419–429, doi:10.1016/j.apsusc.2015.01.163.

[59] G. Jiang, Z. Wei, H. Chen, X. Du, L. Li, Y. Liu, Q. Huang, W. Chen, Preparation of novel carbon nanofibers with BiOBr and AgBr decoration for the photocatalytic degradation of rhodamine B, RSC Adv. 5 (2015) 30433–30437, doi:10.1039/c4ra17290f.

[60] X.J. Wen, C. Zhang, C.G. Niu, L. Zhang, G.M. Zeng, X.G. Zhang, Highly enhanced visible light photocatalytic activity of CeO_2 through fabricating a novel p–n junction BiOBr/CeO_2, Catal. Commun. 90 (2017) 51–55, doi:10.1016/j.catcom.2016.11.018.

[61] X.J. Wang, Y. Zhao, F.T. Li, L.J. Dou, Y.P. Li, J. Zhao, Y.J. Hao, A chelation strategy for in-situ constructing surface oxygen vacancy on {001} facets exposed BiOBr nanosheets, Sci. Rep. 6 (2016) 1–11, doi:10.1038/srep24918.

[62] B. Réti, K. Mogyorósi, A. Dombi, K. Hernádi, Substrate dependent photocatalytic performance of TiO_2/MWCNT photocatalysts, Appl. Catal. A Gen. 469 (2014) 153–158, doi:10.1016/j.apcata.2013.10.001.

[63] S. Yin, J. Di, M. Li, W. Fan, J. Xia, H. Xu, Y. Sun, H. Li, Synthesis of multiwalled carbon nanotube modified BiOCl microspheres with enhanced visible-light response photoactivity, Clean - Soil, Air, Water 44 (2016) 781–787, doi:10.1002/clen.201500418.

[64] B. Weng, F. Xu, J. Xu, Hierarchical structures constructed by BiOX (X = Cl, I) nanosheets on CNTs/carbon composite fibers for improved photocatalytic degradation of methyl orange, J. Nanopart. Res. 16 (2014), doi:10.1007/s11051-014-2766-7.

[65] K. Woan, G. Pyrgiotakis, W. Sigmund, Photocatalytic carbon-nanotube-TiO_2 composites, Adv. Mater. 21 (2009) 2233–2239, doi:10.1002/adma.200802738.

[66] L. Tian, L. Ye, J. Liu, L. Zan, Solvothermal synthesis of CNTs-WO_3 hybrid nanostructures with high photocatalytic activity under visible light, Catal. Commun. 17 (2012) 99–103, doi:10.1016/j.catcom.2011.10.023.

[67] D. Flak, A. Braun, B.S. Mun, J.B. Park, M. Parlinska-Wojtan, T. Graule, M. Rekas, Spectroscopic assessment of the role of hydrogen in surface defects, in the electronic structure and transport properties of TiO_2, ZnO and SnO_2 nanoparticles, Phys. Chem. Chem. Phys. 15 (2013) 1417–1430, doi:10.1039/c2cp42601c.

[68] J. Chen, M. Guan, W. Cai, J. Guo, C. Xiao, G. Zhang, The dominant (001) facet-dependent enhanced visible-light photoactivity of ultrathin BiOBr nanosheets, Phys. Chem. Chem. Phys. 16 (2014) 20909–20914, doi:10.1039/c4cp02972k.

[69] L.M. Yang, G.Y. Zhang, Y. Liu, Y.Y. Xu, C.M. Liu, J.W. Liu, A {110} facet predominated Bi6O6(OH)3(NO3)3·1.5H2O photocatalyst: selective hydrothermal synthesis and its superior photocatalytic activity for degradation of phenol, RSC Adv. 5 (2015) 79715–79723, doi:10.1039/c5ra15629g.

[70] B. Réti, Z. Major, D. Szarka, T. Boldizsár, E. Horváth, A. Magrez, L. Forró, A. Dombi, K. Hernádi, Influence of TiO_2 phase composition on the photocatalytic activity of TiO2/MWCNT composites prepared by combined sol–gel/hydrothermal method, J. Mol. Catal. A Chem. 414 (2016) 140–147, doi:10.1016/J.MOLCATA.2016.01.016.

[71] D. Xiong, T. Fang, L. Yu, X. Sima, W. Zhu, Effects of nano-scale TiO2, ZnO and their bulk counterparts on zebrafish: acute toxicity, oxidative stress and oxidative damage, Sci. Total Environ. 409 (2011) 1444–1452, doi:10.1016/j.scitotenv.2011.01.015.

[72] Z. Pap, K. Mogyorósi, G. Veréb, A. Dombi, K. Hernádi, V. Danciu, L. Baia, Commercial and home-made nitrogen modified titanias. A short reflection about the advantageous/disadvantageous properties of nitrogen doping in the frame of their applicability, J. Mol. Struct. 1073 (2014) 157–163, doi:10.1016/j.molstruc.2014.05.023.